Journal of Materials Chemistry A

Accepted Manuscript

ROYAL SOCIETY OF CHEMISTRY

www.rsc.org/materialsA

Journal Name

RSCPublishing

ARTICLE

Synthesis of Porous Cu_2O/CuO Cages using Cu-based Metal-Organic-Framework as Templates and their Gas-sensing Properties

Cite this: DOI: 10.1039/xoxxoooooox

Received ooth January 2012,
Accepted ooth January 2012

DOI: 10.1039/xoxxoooooox

www.rsc.org/

Yiting Wang, Yinyun Lü, Wenwen Zhan, Zhaoxiong Xie, Qin Kuang,* and Lansun Zheng

Shape-controllable porous, hollow metal oxide cages are attracting more and more attention caused by their widespread applications. In this paper, octahedral, truncated octahedral and cubic Cu_2O/CuO cages were successfully fabricated by the thermal decomposition of the polyhedral crystals of Cu-based metal-organic frameworks (Cu-MOFs) as self-sacrificial templates at 300°C. The morphology of the Cu-MOF polyhedral precursors was well tuned by using lauric acid as the growth modulator under solvothermal conditions. Gas-sensing measurements revealed that the octahedral Cu_2O/CuO cages exhibited a gas-sensing performance far better than those exhibited by truncated octahedral and cubic cages, which is attributed to the cooperative effect of the large specific surface area (150.3 $m^2 \cdot g^{-1}$) and high capacity of surface-adsorbed oxygen of the octahedral Cu_2O/CuO cages.

1. Introduction

Porous, hollow inorganic nanomaterials with well-defined morphologies, also known as cages, have attracted significant attention because of their potential application in many fields, such as gas sensing, energy storage and conversion and catalysis.[1-3] Because of the low cost and high efficiency involved in the fabrication of cages, the self-sacrificial template strategy has stood out from various other synthetic strategies. Obviously, the exploration of appropriate template materials is key for this strategy.

Metal organic frameworks (MOFs) are an emerging class of organic–inorganic hybrid functional materials that are composed of metal ions or metal ion clusters and bridging organic linkers; they have been demonstrated to have promising applications in gas storage and separation, catalysis and drug delivery.[4-7] In recent years, significant efforts have been devoted to exploring new utilization of MOF materials. For example, composite catalysts and sensors have been developed by the combination of high specificity and the precise positioning of MOFs onto different platforms.[8-12] Besides these reports, many attempts have been made to use MOFs as template materials for preparing other functional materials, since they can be transformed to carbons, metals, metal oxides or their hybrid materials via thermolysis under controlled conditions.[13-27] In thermolysis, the organic content of MOFs decomposes into small molecules such as CO_2, H_2O and others, easily leading to the formation of porous, hollow nanostructures while maintaining the geometric shape of the precursors. For this MOF template strategy, both original features (such as exposed facets and thermostability) of the MOF precursors and thermolysis conditions (such as gas atmosphere, temperature, and post-treatment) significantly affect the composition and structure of the final products.[23,26-28] Therefore, the morphology, particle size, composition and surface area of porous nanostructures can be effectively controlled if the abovementioned factors are fully considered in the MOF template strategy.

In contrast to the facilitation in controlling thermolysis conditions, that in controlling the shape of the MOF crystals at the nanoscale, that is, design controlling morphology or exposed crystal facets of MOF crystals without changing material compositions, have been rarely reported.[29-35] This may be caused by the lack of knowledge about the growth mechanisms of MOF crystals. The morphology of MOF crystals cannot be readily predicted according to the relative growth rates of crystals in different orientations caused by complicated topologies.[29] Because of the limited specific faceted MOF crystals, it is difficult to conduct a systematic study to clarify the intrinsic influence of the structural characteristics of the MOF precursors on the nanostructures of the as-fabricated porous metal oxides. Therefore, it is desirable to explore more synthetic routes for acquiring MOF crystals with different shapes.

In this study, we developed a facile solvothermal method to fabricate Cu-based MOF ($[Cu_3(BTC)_2(H_2O)_3]$, HKUST-1) crystals with different polyhedral shapes by using lauric acid (LA) as the growth modulator. The as-synthesized Cu-based MOF crystals were uniform in size, and their morphology evolved from octahedra to truncated octahedra to cube with an increase in the LA concentration. By using these well-defined Cu-MOF polyhedral crystals as template materials, porous and hollow Cu_2O/CuO cages with the same shapes were acquired by simple calcination under appropriate temperatures. Interestingly, we found that the specific surface areas of the as-prepared hollow polyhedral cages are closely related to the thermal stability of the corresponding Cu-MOF templates. In addition, the as-prepared hollow polyhedral cages exhibited good responses towards ethanol, which follows the order of octahedra > cubes > truncated octahedra depending on their specific surface areas.

2. Experimental section

2.1 Chemicals

Copper nitrate trihydrate ($Cu(NO_3)_2{\cdot}3H_2O$), ethanol, acetone, methanol, isopropanol and n-butyl alcohol were purchased from Sinopharm Chemical Regent Co., Ltd. 1,3,5-Benzenetricarboxylic acid (BTC) and LA ($C_{12}H_{24}O_2$) were purchased from J&K Chemistry Technology and Alfa Aesar, respectively. All the reagents were analytically pure and used without further purification.

2.2 Syntheses of samples

HKUST-1 crystals with different morphologies were fabricated by a facile solvothermal route, where LA was used as the shape controlling agent. In a typical synthesis of HKUST-1 octahedra, 41 mg $Cu(NO_3)_2{\cdot}3H_2O$, 24 mg BTC and 1.902 g LA (2.550 g for truncated octahedra; 4.250 g for cubes) were dissolved in 15 mL of n-butyl alcohol in a 25 mL Teflon-lined stainless-steel autoclave, followed by vigorous stirring for 30 min. Then, the autoclave was transferred to an oven and heated at specific temperatures (90 °C for octahedra; 140 °C for truncated octahedra; 120 °C for cubes) for 5 h. The blue product was collected by centrifugation, washed with ethanol three times, and finally dried in a vacuum dryer. It should be stated that the yield of octahedral HKUST-1 obtained from the above LA-assisted solvothermal route was relatively low (*ca.* 10 mg/autoclave), which is far from enough to meet the practical requirements in our study. For this, an alternative synthetic route was adopted to fabricate octahedral HKUST-1 in high yield. First, 0.91 g $Cu(NO_3)_2{\cdot}3H_2O$ and 79 mg BTC were each dissolved in 25 mL of methanol and then the methanolic solution of $Cu(NO_3)_2{\cdot}3H_2O$ was added to that of BTC. After sonication for 10 min, the resulting mixed solution was placed at room temperature for 2 h without stirring. Finally, a large amount of octahedral HKUST-1 products (ca. 120 mg/bottle) was obtained.

The conversion of HKUST-1 into CuO/Cu_2O cages was achieved by calcination in which the as-fabricated HKUST-1 crystals were calcined at 300 °C in a muffle furnace for 1.5–3 h. Finally, black products were obtained. It should be in particular stated that the octahedral CuO/Cu_2O cages for the structure and performance investigations were converted from the octahedral HKUST-1 crystals prepared by the method without LA.

2.3 Characterization and gas-sensing measurement of samples

The morphology of the products was observed by scanning electron microscopy (SEM, Hitachi S4800) and transmission electron microscopy (TEM, JEOL 2100F) with an accelerating voltage of 200 kV. The composition of the products was investigated by powder X-ray diffraction (XRD) on a Rigaku D/max X-ray diffractometer (Cu Kα radiation, λ = 0.15418 nm). Thermogravity (TG) analysis was conducted using an SDT Q600TGA thermal gravimetric analyzer in air flow at a heating rate of 10 °C·min^{-1}. Nitrogen adsorption–desorption isotherms of the products were measured at 77 K on a Tristar II 3020 sorption analyzer (Micromeritics). The specific surface area was determined by the Brunauer–Emmett–Teller (BET) method, and the pore size distribution was calculated by the Barrett–Joyner–Halenda (BJH) method. X-ray photoelectron spectroscopy (XPS) was measured using a Perkin–Elmer model PHI 5600 XPS system from a monochromatic aluminium anode X-ray source with Kα radiation (1486.6 eV), and the spectra were calibrated with the C1s peak at 284.6 eV as the internal standard. Gas-sensing measurements of the as-prepared Cu_2O/CuO hollow cages were conducted on a WS-30A sensor measurement system (Zhengzhou Winsen Electronics Technology, China). The fabrication and testing processes of the sensors have been described in detail in our previous study.[27] The operating temperature was optimized and fixed to 150 °C.

3. Results and discussion

3.1 Controlled synthesis of Cu-MOF polyhedral crystals

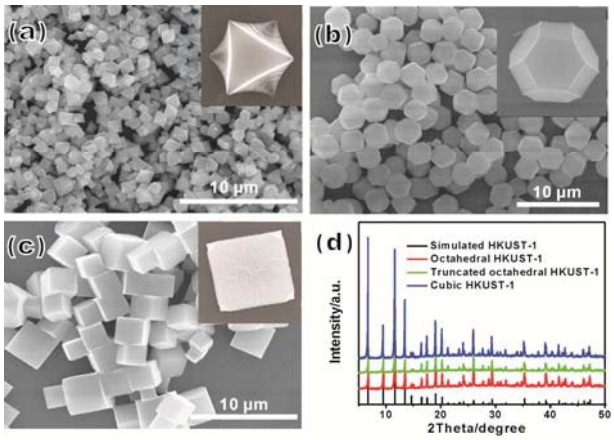

Fig. 1 (a–c) SEM images and (d) XRD patterns of Cu-MOF (HKUST-1) octahedra, truncated octahedra and cubes synthesized with different amounts of LA; the

insets in (a)–(c) show the corresponding high-magnification SEM images of individual particles, which show morphology details.

HKUST-1 ($Cu_3(BTC)_2$), which was first reported by Williams et al., is a polymer framework composed of dimeric cupric tetracarboxylate units (paddle wheels) with aqua molecules coordinating to the axial positions and BTC bridging ligands.[33] This coordination polymer forms face-centred cubic crystals that contain an intersecting three-dimensional (3D) system of large square pores (9 Å by 9 Å). In many cases, HKUST-1 results in octahedral crystals caused by a preference for an increased stability of the (111) surface.[36] To tune the morphology of HKUST-1 crystals, it is necessary to explore a new synthetic strategy. Recently, a so-called coordination modulation strategy has been proposed to achieve the morphology-controlled synthesis of MOFs.[29-32,37] This coordination modulation strategy is based on the use of modulators for modulating the coordination equilibrium by adding capping agents with the same chemical functionality as the linkers to adjust the coordination interactions between metal ions and organic linkers. By doing so, the rates of framework extension and crystal growth are readily controlled, thereby tailoring the size and morphology of the resulting crystals. Carboxylate salts such as sodium formate and sodium acetate are effective modulators for reducing the size of MOF crystals from micrometer to nanometer.[38] The role of carboxylate salts is related to their basicity (increases nucleation rate) and capping groups (COO^-) (prevents crystallites from growing). In our study, LA was used the growth modulator molecules, which has been proven to be highly effective for the rapid microwave-irradiation-assisted syntheses of MOFs.[29]

Figs. 1a–c show SEM images of the HKUST-1 crystals with different morphologies, which were prepared using LA as the shape controlling agent. With increasing LA concentration, the morphology of the as-prepared HKUST-1 crystals clearly evolved from octahedron to truncated octahedron to cubes. The size of the truncated octahedral HKUST-1 crystals is similar to that of cubic HKUST-1 (~2 μm) crystals; on the other hand, the size of the octahedral HKUST-1 crystals is smaller (~1 μm). Fig. 1d shows the XRD patterns of the HKUST-1 crystals. The peaks of all the products match well with the simulated pattern of HKUST-1 ($Cu_3(BTC)_2$), indicating that they are phase-pure.

As is known, the growth of crystals is coordinated by the planes that cooperatively grow at faster and slower speeds, and the exposed facets of the final crystal are usually the planes with slower growth. As a coordination modulator molecule, LA could change the nucleation process of MOF crystals. When LA operates with the framework, the relative energies between the coordination sites on the {111} and {100} faces change with the LA amount, leading to a morphological transition. Under normal conditions, LA prefers the {100} than the {111} face, in which case the energy difference between the faces and the ideal equilibrium state is lower. In the crystal growth process, copper nitrate reacts with LA before the reaction with BTC, and BTC combines with the copper complex prior to copper nitrate, which accelerates the growth of the {100} face. For these reasons, the HKUST-1 crystals are reported to be octahedral. However, the sequence of the energy differences is reserved when large amounts of LA are introduced, leading to the appearance of cubic crystals. Truncated octahedra will be formed if the energy differences are balanced.[29]

3.2 Conversion of the Cu-MOF polyhedra into the hollow Cu_2O/CuO cages

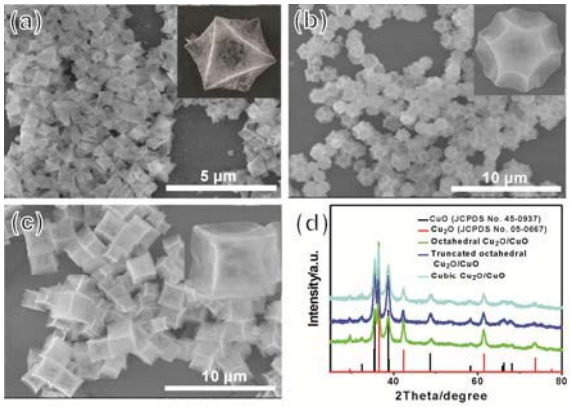

Fig. 2 SEM images of as-prepared Cu_2O/CuO cages with different morphologies: (a) octahedra, (b) truncated octahedra (c) cube; insets in (a)–(c) show magnified images; (d) XRD patterns of three Cu_2O/CuO cages.

The conversion of Cu-MOF polyhedra into hollow oxide cages was achieved by calcination at 300 °C. Given the low output of the octahedral precursors in the LA-assisted synthetic method, the octahedral HKUST-1 crystals prepared by an alternative synthetic route without LA, which possess highly similar characteristic to the octahedral one by the LA-assisted method in morphology and size, were used in our study (see Fig. S1, ESI†). Figs. 2a–c show the SEM images of the as-prepared Cu_2O/CuO cages, where the morphologies of the products after calcination can be observed. The insets in each image show high-magnification SEM images. As expected, the template morphologies are well preserved in all the products, and their sizes are approximately consistent with those of their corresponding precursors, implying that no severe shrinkage occurs. Compared to the HKUST-1 precursors, the calcination products become slightly transparent under the electron beam of SEM, and the surfaces clearly turn concave because of the structural shrinkage caused by the loss of organic components. From the insets in Figs. 2a–c, the holes appear on the surface of octahedral particles more frequently than on the surface of truncated octahedra and cubes. The XRD patterns (Fig. 2d) indicate that all calcination products are mixtures of CuO (JCPDS No.45-0937) and Cu_2O (JCPDS No.05-0067). The diffraction peaks of these products are not only weak but also slightly broaden, suggesting that the products are poor in crystallinity and formed with primary crystallites of CuO and Cu_2O. To ascertain the complete decomposition of the Cu-MOF templates, the element analysis was further conducted. The contents of remnant carbon in the octahedral, truncated octahedral and cubic products are 2.26%, 0.20%, and 0.63%, respectively, implying that conversion is completed at 300 °C.

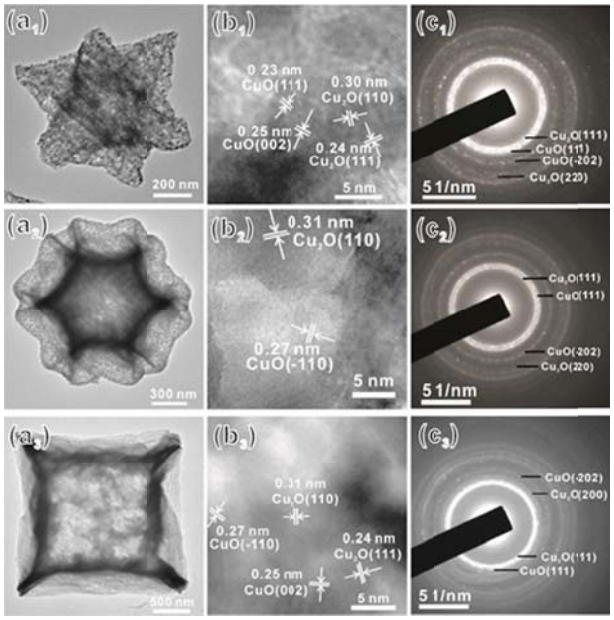

Fig. 3 (a_{1-3}) Low-magnification TEM images, (b_{1-3}) HRTEM images and (c_{1-3}) SAED patterns of individual Cu_2O/CuO cages with polyhedral morphologies: (1) octahedra, (2) truncated octahedra (3) cubes.

Fig. 3 shows transmission electron microscopy (TEM) images of the calcination products, depicting the interior structure. As shown in Figs. $3a_{1-3}$, the obtained particles exhibiting well-defined polyhedral morphologies are actually hollow, and several tiny pores are distributed in each particle. Compared to the truncated octahedral and cubic particles, the octahedral particles have more loose pores. From high-resolution TEM images (HRTEM, Fig. $3b_{1-3}$), these hollow polyhedral particles are clearly formed with many primary crystallites having a size of 10–15 nm, which is consistent with XRD analysis. For all samples, two groups of lattice fringes, which can be assigned as Cu_2O and CuO according to their interlayer spacings, respectively, are observed on adjacent primary crystallites. Besides these fringes, ring-like diffraction patterns of both Cu_2O and CuO are observed in the corresponding selected area electron diffraction (SAED) patterns (Fig. $3c_{1-3}$). These results indicate that the as-prepared hollow polyhedra are composites containing randomly attached Cu_2O and CuO crystallites.

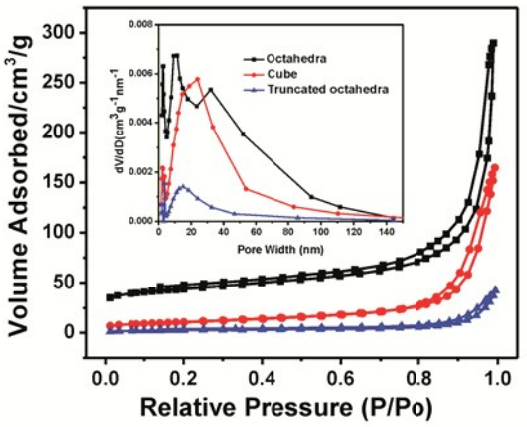

Fig. 4 N_2 adsorption–desorption isotherms and pore size distributions (inset) of the Cu_2O/CuO polyhedral cages.

To examine the pore characteristics of the as-prepared polyhedral cages, N_2 adsorption–desorption isotherms and BJH pore size distribution analysis at 77 K were conducted. As shown in Fig. 4, the three polyhedral cages show a type III adsorption isotherm, which is characterized by the convex shape in the whole range of relative pressures and can be observed when lateral interactions between adsorbed molecules are strong in comparison to interactions between the adsorbent surface and adsorbate.[39] When the relative pressure (P/P_0) is low, the amount of N_2 adsorbed is low. However, the amount of adsorbed N_2 increases with P/P_0, and the amount of adsorbed N_2 rapidly increases and reaches a plateau as soon as P/P_0 reaches 0.8. Noticeably, the trend becomes clear at a relatively large specific surface area. An H3-type hysteresis loop over a relative pressure range of $0.7 < P/P_0 < 1.0$ is observed, which is usually attributed to slitlike pores of the aggregates (loose assemblages) comprised of primary particles.[39] Notably, there are significant differences between the polyhedral cages with respect to their specific surface areas and pore distributions. According to our multiple BET measurements, the specific surface areas of the three hollow cages are 150.3 ± 10.0 $m^2 \cdot g^{-1}$, 8.5 ± 2.0 $m^2 \cdot g^{-1}$ and 35.0 ± 5.0 $m^2 \cdot g^{-1}$ for the octahedral, truncated octahedral and cubic Cu_2O/CuO cages, respectively. As shown in the inset of Fig. 4, in addition, the octahedral Cu_2O/CuO cages have three pore size distributions with the maximum peaks at 2.8, 10 and 32 nm, respectively. The two relatively small-sized pores probably originate from the pores on the cage shells; however, the larger pores correspond to the holes between the different cages. In contrast, the cubic Cu_2O/CuO cages only exhibit a pore size with the maximum distributions around 24 nm. Nevertheless, the pore size distribution of the truncated octahedral Cu_2O/CuO cages in the range below 10 nm is almost negligible, indicating that there are few pores on the cage shells. Notably, these structural characteristics about the specific surface areas and pore distributions are consistent with the observation results in Fig. 3 where the octahedral cages appear to be looser and possess more pores. As far as we know, the specific surface area (150.3

± 10 $m^2 \cdot g^{-1}$) of the porous octahedral Cu_2O/CuO cages is far higher than that of most of the previously reported porous Cu_2O or CuO nanostructures, which are usually in the range of 10–70 $m^2 \cdot g^{-1}$.[16,20,38,40-43] Obviously, the superiority of the octahedral cages with respect to their specific surface area is attributed to a combination of highly porous and hollow structures.

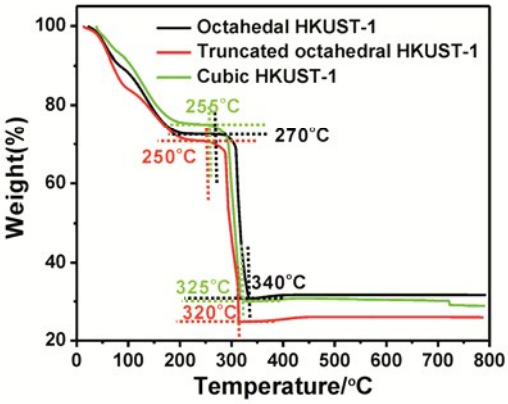

Fig. 5 TG–DSC curves of HKUST-1 precursors.

In thermal decomposition, temperature is well known to be a key factor for ensuring that the shape of the as-formed products is well maintained with that of the templates. If the calcination temperature is very low, the organic components will not be completely decomposed. In contrast, if the calcination temperature is very high, the produced gaseous molecules will be released too fast such that the structure of the hollow cages will be ruined, thereby resulting in a decrease of the specific surface area. To clarify the possible influence of calcination on the structure of the as-prepared Cu_2O/CuO cages, TG measurements of the HKUST-1 polyhedral crystals were recorded under air. TG curves in Fig. 5 reveal that the weight loss behaviour of HKUST-1 can be divided into two major stages. The first weight loss stage occurs at temperatures below 200 °C, which is attributed to the removal of water, modulator (LA) and solvent molecules from the surfaces and pores of HKUST-1 precursors. Note that, for the three HKUST-1 polyhedral crystals, there is a plateau stage before a sharp weight loss further occurs. This indicates that the frameworks of the HKUST-1 crystals with solvent removed remain stable in this temperature range. Interestingly, the three HKUST-1 polyhedral crystals display different onset decomposition temperatures of the frameworks. For the octahedral HKUST-1 crystals, the second weight loss starts at around 270 °C and ends around 340 °C. According to our calculation, the relative weight loss (weight loss/residual weight × 100%) of the three HKUST-1 crystals at this stage is approximately 60%, roughly corresponding to the theoretical weight loss caused by the burning of the organic ligands in HKUST-1 in air (around 64% for the reaction $Cu_3(BTC)_2 \rightarrow Cu_2O$ and 60% for the reaction $Cu_3(BTC)_2 \rightarrow$ CuO). Notably, with increasing temperature, a slight weight increase of approximately 1% is observed in the temperature range from 330 °C to 450 °C, which is attributed to the oxidation of Cu_2O in air ($Cu_2O + 1/2O_2 \rightarrow 2CuO$). Interestingly, the truncated octahedral and cubic HKUST-1 polyhedra exhibit thermostability different from that of the octahedral sample. According to the starting and ending decomposition temperatures, the three HKUST-1 crystals follow the thermostability order of truncated octahedra < cubes < octahedra. For the truncated octahedra, the $[Cu_3(BTC)_2]$ framework can only be preserved at 250 °C, which is lower than that of the octahedral HKUST-1 crystals by approximately 15 °C. Of note, previous study has demonstrated that for HKUST-1 crystals with identically octahedral morphology, the onset decomposition temperature of the frameworks is not affected by different types of solvents in the pores.[44] Given that, it seems reasonable that the difference of the specific surface areas of the as-prepared Cu_2O/CuO cages primarily stems from the difference of HKUST-1 crystals enclosed with different facets in thermostability. Obviously, the pore sizes of the {111} and {100} facets of HKUST-1 precursors are different, which would lead to different releasing rates of gaseous decomposed products (H_2O and CO_2), thereby producing distinct porous structures and surface areas of polyhedral Cu_2O/CuO cages. Of note, the calcination temperature of 300 °C is appropriate for the octahedral HKUST-1 precursors. In contrast, for the truncated octahedral precursors, the H_2O and CO_2 gases produced from thermal decomposition are released at a faster rate, which severely destroys the structure of the final Cu_2O/CuO cages, thereby leading to the lowest specific surface area. In fact, the Cu_2O/CuO cages would be severely structurally destroyed when the calcination temperature were elevated to a higher temperature, *e.g.* 350 °C (Fig. S2, ESI†).

3.3 Gas-sensing performances of the Cu_2O/CuO cages with different morphologies

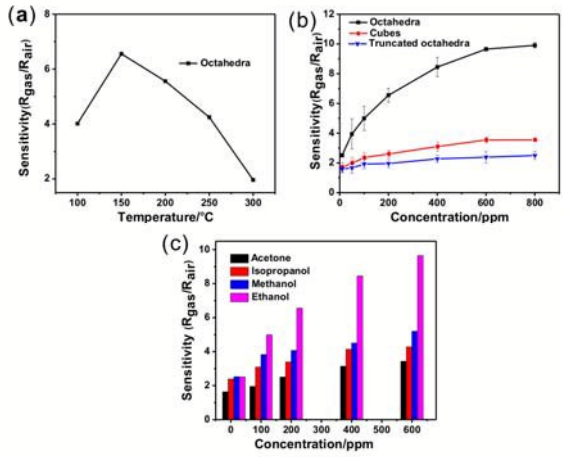

Fig. 6 (a) Temperature-dependent sensitivity curve of the octahedral Cu_2O/CuO cages towards 200 ppm ethanol; (b) concentration sensitivity curves of the three samples; (c) concentration sensitivity bar graph of the octahedral Cu_2O/CuO cages measured with different detected gases.

As traditional p-type semiconductors, both Cu_2O and CuO play significant roles in gas sensing, and their composite

nanomaterials have been demonstrated to exhibit superior sensing performances compared to individual components, caused by the presence of an additional depletion layer at the interface.[38,42-43,45-46] Considering significant advantages of porous and hollow structures as well as homogeneous heterojunctions in gas sensing, the as-prepared Cu_2O/CuO polyhedral cages are anticipated to exhibit superior performance in gas sensing.

In our study, ethanol was chosen as the primary detected gas for its widespread use in daily life and well-understood sensing mechanism.[47,48] Before testing, it is essential to find out an optimal operating temperature for the as-prepared Cu_2O/CuO cages. As shown in Fig. 6a, the highest sensitivity (S = 6.6) appears at 150 °C for the octahedral Cu_2O/CuO sample when 200 ppm ethanol was used as the detected gas. According to previous reports, the optimal operating temperature of sensors based on Cu_2O, CuO or their composites is mostly in the range of 150–300 °C, which varies with the detected gases and fabrication techniques of the sensors (see Table S1 in the supporting information).[-38,40,42,43,45,46,48-52] Therefore, the Cu_2O/CuO hollow cages with a relatively low operating temperature show a great advantage on account of reducing energy consumption. Fig. 6b shows concentration-dependent sensitivity curves of the three Cu_2O/CuO hollow cages at an operating temperature of 150 °C. The sensitivity of the sensors increases with increasing ethanol concentration, and it almost reaches a plateau at 600 ppm. The curves demonstrate a significant difference between these three samples. Among the three samples, the octahedral Cu_2O/CuO cages perform the best, followed by cubic cages, with the worst performance by the truncated octahedral cages. This order well agrees with that of the abovementioned BET surface area, which is mainly caused by the fact that the larger surface area can offer more active sites for interaction with the detected gases. However, the sensing performance of the as-prepared octahedral Cu_2O/CuO cage is just above average compared to other relevant reports listed in Table S1. Obviously, the sensing performance of the samples is restricted by their relatively poor crystallinity.

For sensors, selectivity is another critical parameter for evaluating the gas sensing performance. Therefore, in addition to ethanol, methanol, isopropanol and acetone were further detected in our study, in view of their similar response mechanism. Fig. 6c compares concentration-dependent sensitivities of the octahedral Cu_2O/CuO cages to ethanol, methanol, isopropanol and acetone. For the four detected gases with the same concentration, the sensitivity of the octahedral cages follows the sequence of ethanol > methanol > isopropanol > acetone. This means that the octahedral Cu_2O/CuO cages demonstrate promising potential for ethanol with high selectivity. With respect to reducibility, acetone is significantly weaker than alcohols, and because of the alkyl group, alcohols exhibit distinguishable reducibility.

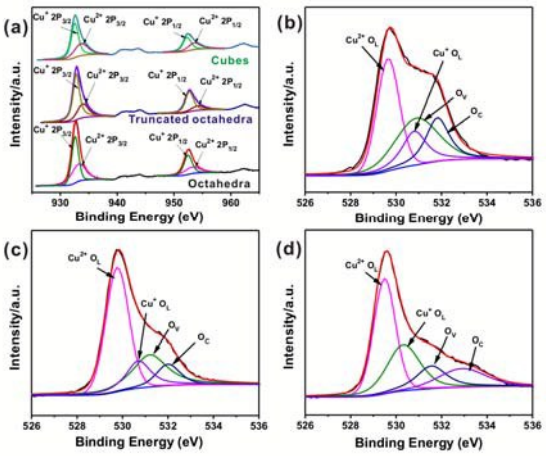

Fig. 7 (a) Cu2p XPS spectra and (b–d) O1s XPS spectra of three Cu_2O/CuO samples: (b) Octahedra, (c) Cubes, (d) Truncated octahedra

Notably, besides the specific surface area, the surface state of sensing materials, which varies depending upon the adsorbent species, plays key roles in gas sensing. When O_2 is adsorbed on the metal oxide surface, the electrons inside the metal oxides are delivered to O_2, forming an electronic depletion layer on the oxide surface, resulting in a charge transport barrier between particles. When the semiconductor surface is exposed to the detected gas, the thickness of the electronic depletion layer of the sensing material significantly changes. This surface state change can be translated into the electrical signals during gas-sensing measurements. To acquire information about the surface state of the as-prepared Cu_2O/CuO polyhedral cages, XPS was conducted. As shown in Fig. 7a, the three samples display similar Cu 2p XPS spectra, where two main peaks are observed at 952.5 ± 0.2 eV and 932.7 ± 0.1 eV, respectively, corresponding to the $2p_{1/2}$ and $2p_{3/2}$ peaks of Cu. Judging from the positions, the two main peaks mainly originate from Cu^+, rather than from Cu^{2+}, because XPS peaks of Cu^{2+} usually appear at higher energy positions (953.6± 0.4 eV and 933.6 ± 0.3 eV).[53,54] However, some satellite peaks corresponding to electronic shake-up are observed in the Cu 2p XPS spectra of the three samples, accompanied by $2p_{1/2}$ and $2p_{3/2}$ peaks. The presence of the satellite peaks proves the existence of CuO on the cage surface, because of their absence in Cu_2O.[54,55] Therefore, both Cu_2O and CuO coexist on the surface of these hollow cages. Fig. 7b–d show the O1s XPS spectra of the three samples. Notably, every O1s curve is asymmetric and can be resolved into four components by Gaussian fitting, *i.e.* lattice oxygen of Cu_2O and CuO ($O_L(Cu^+)$ and $O_L(Cu^{2+})$), oxygen vacancy (O_V) and adsorbed oxygen (O_C). The O_C component of high binding energy (531.8–532.9 eV) is usually attributed to chemisorbed and dissociated oxygen species (O_2^-, O^{2-} or O^-) and OH^-. Thus, we can estimate the oxygen adsorption ability of different samples according to the relative proportion of O_C in the XPS O1s peaks. Table 1 lists the results of each oxygen component in the three samples. The relative proportion of O_C in the samples is 18.3%, 10.4% and

15.4% for the octahedral, cubic and truncated octahedral Cu_2O/CuO cages, respectively. This indicates that the octahedral Cu_2O/CuO cages exhibit the strongest ability for adsorbing oxygen, followed by the truncated octahedral and cubic cages. Note that this sequence does not match the performances of the three samples for gas sensing. As mentioned above, the gas sensing ability of semiconductor materials is related to both the specific surface area and amount of the external O_C species. With respect to the specific surface area, the truncated octahedral cages are far lower than the octahedral and cubic cages. Under the combined effect of both specific surface area and capacity, the octahedral cages perform the best for gas sensing, followed by cubic and truncated octahedral cages.

Table 1. Results of curve fitting of O 1s XPS spectra of the different samples

Oxygen species		Octahedra	Cube	Truncated octahedra
O_C	Binding energy (eV)	531.8	532.0	532.9
	Percentage (%)	18.3	10.4	15.4
O_V	Binding energy (eV)	531.0	531.2	531.6
	Percentage (%)	31.3	25.6	14.4
O_L	Binding energy (eV)	530.8 (Cu^+) 529.7 (Cu^{2+})	530.7 (Cu^+) 529.8 (Cu^{2+})	530.3 (Cu^+) 529.5 (Cu^{2+})
	Percentage (%)	50.4	64.0	70.2

4. Conclusion

In summary, the porous Cu_2O/CuO cages with different polyhedral morphologies were successfully synthesized by the thermal decomposition of HKUST-1 precursors. These porous cages were actually composed of numerous primary crystallites of Cu_2O and CuO. The as-prepared octahedral Cu_2O/CuO cages exhibited the largest surface area (150.3 $m^2 \cdot g^{-1}$), while the truncated octahedral cages exhibited the smallest one (9.8 $m^2 \cdot g^{-1}$). Taking advantage of their porosity, the as-prepared cages were applied as gas sensing materials. Because of the larger surface area, the octahedral Cu_2O/CuO cages exhibited superior performance in gas sensing tests with high sensitivity and exhibited good selectivity to ethanol as compared to the truncated octahedral and cubic Cu_2O/CuO cages. This study describes an economical and simple method for fabricating other porous metal oxides with well-defined structures, which can be used in catalysis, lithium ion batteries and energy storage.

Acknowledgements

This work was supported by the National Basic Research Program of China (2011CBA00508), the National Natural Science Foundation of China (21171142, 21473146, and 21333008), and the program for New Century Excellent Talents in University (NCET-11-0294).

Notes and references

State Key Laboratory of Physical Chemistry of Solid Surfaces & Department of Chemistry, College of Chemistry and Chemical Engineering, Xiamen University, Xiamen, 361005, People's Republic of China. Email: qkuang@xmu.edu.cn

1. M. H. Oh, T. Yu, S. H. Yu, B. Lim, K. T. Ko, M. G. Willinger, D. H. Seo, B. H. Kim, M. G. Cho, J. H. Park, K. Kang, Y. E. Sung, N. Pinna and T. Hyeon, *Science*, 2013, **340**, 964−968.
2. L. Wang, F. Tang, K. Ozawa, Z. G. Chen, A. Mukherj, Y. Zhu, J. Zou, H. M. Cheng and G. Q. Lu, *Angew. Chem. Int. Ed.*, 2009, **48**, 7048−7051.
3. Z. Wang, L. Zhou and X. W. Lou, *Adv. Mater*, 2012, **24**, 1903−1911.
4. K. Ke, Y. P. Yuan, L. G. Qiu, Y. H. Shen, A. J. Xie, J. F. Zhu, X. Y. Tian and L. D. Zhang, *J. Mater. Chem.*, 2011, **21**, 3843−3848.
5. A. R. Millward and O. M. Yaghi, *J. Am. Chem. Soc.*, 2005, **127**, 17998−17999.
6. X. Dong, K. Huang, S. Liu, R. Ren, W. Jin and Y. S. Lin, *J. Mater. Chem.*, 2012, **22**, 19222.
7. I. Luz, F. X. Llabrés i Xamena and A. Corma, *J. Cata.*, 2010, **276**, 134-140.
8. S. Li, W. Shi, G. Lu, S. Li, S. C. Loo and F. Huo, *Adv Mater.*, 2012, **24**, 5954−5958.
9. G. Lu, S. Li, Z. Guo, O. K. Farha, B. G. Hauser, X. Qi, Y. Wang, X. Wang, S. Han, X. Liu, J. S. DuChene, H. Zhang, Q. Zhang, X. Chen, J. Ma, S. C. J. Loo, W. D. Wei, Y. Yang, J. T. Hupp and F. Huo, *Nat. Chem.*, 2012, **4**, 310−316.
10. R. Ameloot, E. Gobechiya, H. Uji-i, J. A. Martens, J. Hofkens, L. Alaerts, B. F. Sels and D. E. D. Vos, *Adv. Mater.*, 2010, **22**, 2685–2688.
11. R. Ameloot, L. Stappers, J. Fransaer, L. Alaerts, B. F. Sels and D. E. D. Vos, *Chem. Mater.*, 2009, **21**, 2580–2582.
12. W. W. Zhan, Q. Kuang, J. Z. Zhou, X. J. Kong, Z. X. Xie and L. S. Zheng, *J. Am. Chem. Soc.*, 2013, **135**, 1926−1933.
13. J. K. Sun and Q. Xu, *Energy Environ. Sci.*, **2014**, *7*, 2071–2100.
14. A. Banerjee, R. Gokhale, S. Bhatnagar, J. Jog, M. Bhardwaj, B. Lefez, B. Hannoyer and S. Ogale, *J. Mater. Chem.*, 2012, **22**, 19694–19699.
15 A. S. Hall, A. Kondo, K. Maeda and T. E. Mallouk, *J. Am. Chem. Soc.*, 2013, **135**, 16276−16279.
16. L. Hu, Y. Huang, F. Zhang and Q. Chen, *Nanoscale*, 2013, **5**, 4186−4190.
17. L. Hu, P. Zhang, Y. Sun, S. Bao and Q. Chen, *Chemphyschem*, 2013, **14**, 3953−3959.
18. Z. Jiang, Z. Li, Z. Qin, H. Sun, X. Jiao and D. Chen, *Nanoscale*, 2013, **5**, 11770−11775.
19. T. K. Kim, K. J. Lee, J. Y. Cheon, J. H. Lee, S. H. Joo and H. R. Moon, *J. Am. Chem. Soc.*, 2013, **135**, 8940−8946.
20. R. Wu, X. Qian, F. Yu, H. Liu, K. Zhou, J. Wei and Y. Huang, *J. Mater. Chem. A*, 2013, **1**, 11126−11129.
21. L. Zhang, H. B. Wu and X. W. Lou, *J. Am. Chem. Soc.*, 2013, **135**, 10664−10672.

22. W. Chaikittisilp, K. Ariga and Y. Yamauchi, *J. Mater. Chem. A*, 2013, **1**, 14−19.
23. N. L. Torad, M. Hu, S. Ishihara, H. Sukegawa, A. A. Belik, M. Imura, K. Ariga, Y. Sakka and Y. Yamauchi, *Small*, 2014, **10**, 2096−2107.
24. Z. Wang, X. Li, H. Xu, Y. Yang, Y. Cui, H. Pan, Z. Wang, B. Chen and G. Qian, *J. Mater. Chem. A*, 2014, **2**, 12571−12575.
25. F. Zou, X. L. Hu, Z. Li, L. Qie, C. C Hu, R. Zeng, Y. Jiang and Y. H. Huang, *Adv. Mater.*, 2014, **26** 6622−6628.
26. L. Zhang, H. B. Wu, S. Madhavi, H. H. Hng and X. W. Lou, *J. Am. Chem. Soc.*, 2012, **134**, 1388−17391.
27. Y. Y. Lu, W. W. Zhan, Y. He, Y. T. Wang, X. J. Kong, Q. Kuang, Z. X. Xie and L. S. Zheng, *ACS Appl. Mater. Interfaces*, 2014, **6**, 4186−4195.
28. X. Xu, R. Cao, S. Jeong and J. Cho, *Nano Lett.*, 2012, **12**, 4988−4991.
29. A. Umemura, S. Diring, S. Furukawa, H. Uehara, T. Tsuruoka and S. Kitagawa, *J. Am. Chem. Soc.*, 2011, **133**, 15506−15513.
30. J. M. Yang, Q. Liu, Y. S. Kang and W. Y. Sun, *Dalton Trans.*, 2014, **43**, 16707−16712.
31. D. Li, H. Wang, X. Zhang, H. Sun, X. P. Dai, Y. Yang, L. Ran, X. S. Li, X. Y. Ma and D. W. Gao, *Cryst. Growth Des.*, 2014, **14**, 5856–5864.
32. M. Sindoro, A. Y. Jee and S. Granick, *Chem. Commun.*, 2013, **49**, 9576−9578.
33. S. S. Chui, S. M. Lo, J. P. H. Charmant, A. G. Orpen and I. D. Williams, *Science*, 1999, **283**, 1148−1150.
34. Y. Pan, D. Heryadi, F. Zhou, L. Zhao, G. Lestari, H. Su and Z. Lai, *CrystEngComm.*, 2011, **13**, 6937−6940.
35. M. Pang, A. J. Cairns, Y. Liu, Y. Belmabkhout, H. C. Zeng and M. Eddaoudi, *J. Am. Chem. Soc.*, 2012, **134**, 13176−13179.
36. S. Amirjalayer, M. Tafipolsky and R. Schmid, *J. Phys. Chem. Lett.*, 2014, **5**, 3206−3210
37. T. Tsuruoka, S. Furukawa, Y. Takashima, K. Yoshida, S. Isoda and S. Kitagawa, *Angew. Chem. Int. Ed.*, 2009, **48**, 4739−4743.
38.
38. F. N. Meng, X. P. Di, H. W. Dong, Y. Zhang, C. L. Zhu, C. Li and Y. J. Chen, *Sens. Actuat. B*, 2013, **182**, 197−204.
39.
39. M. Kruk and M. Jaroniec, Chem. Mater., 2001 **13**, 3169−3183.
40. H. Xu, G. Zhu, D. Zheng, C. Xi, X. Xu and X. Shen, *J. Colloid Interf. Sci.*, 2012, **383**, 75−81.
41. L. Xu, L. P. Jiang and J. J. Zhu, *Nanotechnology*, 2009, **20**, 045605.
42. L. J. Zhou, Y. C. Zou, J. Zhao, P. P. Wang, L. L. Feng, L. W. Sun, D. J. Wang and G. D. Li, *Sens. Actuat. B*, 2013, **188**, 533−539.
43. C. Yang, F. Xiao, J. D. Wang and X. T. Su, *Sens. Actuat. B*, 2015, **207**, 177−185.
44. Y. Yang, P. Shukla, S. Wang, V. Rudoph, X M. Chen and Z. Zhu, *RSC Adv.* 2013, **3**, 17065−17072.
45. J. Zhang, J. Liu, Q. Peng, X. Wang and Y. Li, *Chem. Mater.*, 2006, **18**, 867−871.
46. L. Zhang, Z. Cui, Q. Wu, D. Guo, Y. Xu and L. Guo, *CrystEngComm*, 2013, **15**, 7462−7467.
47. S. Julia, A. Nururddin, S. Nugraha and B. Yuliarto, *AIP Conf. Proc*, 2011, **1415**, 205−208.
48. Y. Sui, Y. Zeng, W. Zheng, B. Liu, B. Zou and H. Yang, *Sens. Actuat. B*, 2012, **171-172**, 135−140.
49. H. G. Zhang, Q. S. Zhu, Y. Zhang, Y. Wang, L. Zhao and B. Yu, *Adv. Funct. Mater.*, 2007, **17**, 2766−2771.
50. X. Wan, J. Wang, L. Zhu and J. Tang, *J. Mater. Chem. A*, 2014, **2**, 13641−13647.
51. A. Aslani and V. Oroojpour, *Phys. B*, 2011, **406**, 144−149.
52. D. P. Volanti, A. A. Felix, M. O. Orlandi, G. Whitfield, D. J. Yang, E. Longo, H. L. Tuller and J. A. Varela, *Adv. Funct. Mater,* 2013, **23**, 1759−1766.
53. M. P. Hernández, J. F. Fernández-Bertrán, M. H. Farías and J. A. Díaz, *Surf. Interface Anal.*, 2007, **39**, 434−437.
54. P. Jiang, D. Prendergast, F. Borondics, S. Porsgaard, L. Giovanetti, E. Pach, J. Newberg, H. Bluhm, F. Besenbacher and M. Salmeron, *J. Chem. Phys.*, 2013, **138**, 024704.
55. H. Azimi, S. Kuhri, A. Osvet, G. Matt, L. S. Khanzada, M. Lemmer, N. A. Luechinger, M. I. Larsson, E. Zeira, D. M. Guldi and C. J. Brabec, *J. Am. Chem. Soc.*, 2014, **136**, 7233−7236.

Graphical Abstract

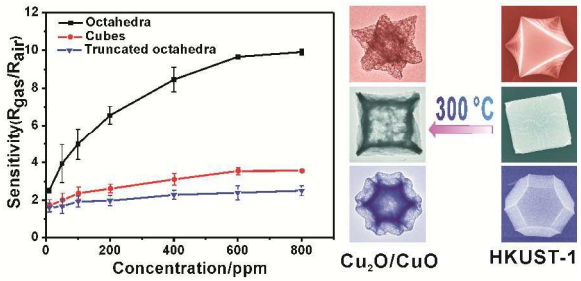

Porous Cu_2O/CuO polyhedral cages with excellent gas-sensing properties were successfully fabricated by thermal decomposition of Cu-based metal-organic frameworks polyhedral crystals.